

## Ground state proton capture reactions from 20 to 100 MeV

H. J. Hausman, S. L. Blatt, T. R. Donoghue, J. Kalen, W. Kim, D. G. Marchlenski,  
T. W. Rackers, and P. Schmalbrock

*Department of Physics, The Ohio State University, Columbus, Ohio 43210*

M. A. Kovash

*Department of Physics, University of Kentucky, Lexington, Kentucky 40506*

A. D. Bacher

*Department of Physics, Indiana University, Bloomington, Indiana 47401*

(Received 27 July 1987)

Proton capture reactions on targets of  $^{11}\text{B}$ ,  $^{12}\text{C}$ ,  $^{15}\text{N}$ ,  $^{16}\text{O}$ , and  $^{27}\text{Al}$  were measured from  $E_p = 20$  to 100 MeV. The energy dependence of the  $\theta_\gamma = 60^\circ$  differential cross sections are presented for captures populating the ground states of  $^{12}\text{C}$ ,  $^{13}\text{N}$ ,  $^{16}\text{O}$ ,  $^{17}\text{F}$ , and  $^{28}\text{Si}$ . Differential-cross-section and analyzing-power angular distributions are presented at bombarding energies of  $E_p = 20.8$ , 28.35, 49.2, and 49.69 MeV. Calculations from two capture-reaction models are compared to the data.

### I. INTRODUCTION

This paper reports on proton capture reactions on targets of  $^{11}\text{B}$ ,  $^{12}\text{C}$ ,  $^{15}\text{N}$ ,  $^{16}\text{O}$ , and  $^{27}\text{Al}$  populating the ground state of  $^{12}\text{C}$ ,  $^{13}\text{N}$ ,  $^{16}\text{O}$ ,  $^{17}\text{F}$ , and  $^{28}\text{Si}$  over proton bombarding energies from 20 to 100 MeV. The experiments were performed at the Indiana University Cyclotron Facility (IUCF) utilizing the pulsed polarized proton beam. Discrimination between the large neutron background and the high-energy  $\gamma$  rays of interest was accomplished by time-of-flight techniques. By utilizing cosmic-ray rejection, pulse pileup rejection, and fast electronics, we were also able to observe proton captures populating highly excited states in the residual nuclei; as an example we have observed strongly populated states in  $^{12}\text{C}$  at excitations as high as 19 MeV.<sup>1</sup> In a previous publication,<sup>2</sup> we reported on the existence of a giant resonance built on the cluster of final states in  $^{12}\text{C}$  at that energy. In a simple single-particle picture, the resonance arises from 1p-1h configurations with the particle at  $2\hbar\omega$  excitation, while the final state after  $\gamma$  decay has the particle at  $1\hbar\omega$ . Following this work, Anghinolfi *et al.*<sup>3</sup> reported the observation of giant resonances built on many of the lower excited states of  $^{12}\text{C}$ ; the Brookhaven National Laboratory/University of Washington collaboration<sup>4</sup> reported similar results in the  $^{27}\text{Al}(p,\gamma)^{28}\text{Si}$  reaction.

Over the past few years we have been investigating proton capture reactions on a variety of targets over the energy range reported on here. While one of the purposes of the experiments was to explore particular aspects of proton capture reactions at medium energies, and especially to study proton capture to highly excited states, we have accumulated a considerable amount of data on ground-state captures as well. It is the purpose of this report to provide energy-dependence data sets on ground-state captures which supplement data sets from

the inverse  $(\gamma,p)$  reactions already published in this energy range.<sup>5,6</sup> We have also measured some cross-section and analyzing-power angular distributions; the latter should provide a more stringent test than the cross-section angular distributions for theoretical treatments of various capture reaction models.

Empirical direct-semidirect (DSD) models have given good agreement with capture measurements at energies below 30 MeV. We have extended these calculations to the region above 30 MeV to compare with our data. In addition we include some calculations from another direct-capture model, based on the use of the Dirac equation, which includes meson-exchange terms.

### II. EXPERIMENTAL PROCEDURE

Protons from the IUCF cyclotron were used to bombard gaseous targets of  $^{15}\text{N}$  and  $^{16}\text{O}$  and solid targets of  $^{11}\text{B}$ ,  $^{12}\text{C}$ , and  $^{27}\text{Al}$ . The naturally occurring oxygen gas and the 99% enriched  $^{15}\text{N}$  gas were enclosed in a thin-walled cylindrical brass gas cell, 2.41 cm long and 1.91 cm in diameter, with  $6.35 \times 10^{-4}$  cm Havar foils as entrance and exit windows. Typical gas-cell pressures were  $2 \times 10^5$  to  $3.1 \times 10^5$  Pa. Background spectra from the gas target assembly were obtained by evacuating the cell after each gas run. The  $^{27}\text{Al}$  targets were self-supporting foils of natural aluminum of 99.35% purity and ranged from 13.22 to 41 mg/cm<sup>2</sup> for various runs. The boron targets were enriched to 97.1%  $^{11}\text{B}$  and the carbon targets to 99.9% in  $^{12}\text{C}$ . Target thicknesses in these two cases ranged between 25 and 35 mg/cm<sup>2</sup> for various runs.

The emitted gamma rays were detected by the Ohio State University Medium Energy Gamma Assembly,<sup>1</sup> consisting of a 25-cm diam by 30 cm long NaI(Tl) crystal surrounded by a plastic annulus. The annulus served as an anticoincidence shield for background and

cosmic-ray rejection and also to give a measure of escaped radiation from the NaI crystal. The detector was positioned some 1 m from the target and subtended a solid angle of 9.16 msr. The detector resolution was about 3.5% full width at half maximum (FWHM) at  $E_\gamma = 45$  MeV. The detector system utilizes time-of-flight information to reject neutron-induced events; the time resolution was 2.3 ns and provided good discrimination between  $\gamma$ -ray and neutron events at all bombarding energies. At beam currents from 10 to 50 nA, total counting rates in the NaI crystal were as high as  $2 \times 10^5$  per second. Pileup rejection circuitry was incorporated into the NaI channel to eliminate virtually all spectral distortion from this source. A photomultiplier gain-stabilization circuit<sup>7</sup> employing light-emitting diodes (LED's), capable of operating at rates over  $3 \times 10^5$  pulses per second, maintained gain stability to within  $\pm 1\%$  over runs extending from 4 to 8 h in duration. In Fig. 1 we show the effect of the various conditions on our spectra. In the upper spectrum, curve (a) represents the total yield in our detector with no subsequent conditions; a discriminator cutoff was placed at  $E_\gamma \sim 10$  MeV. Curve (b) shows the same spectrum when the time-of-flight condition, discriminating  $\gamma$  rays from neutrons, is enabled. The time-of-flight spectrum itself is shown in the lowest section of the figure. In the middle box of Fig. 1 is a blown-up spectrum of (b) appearing in the top box. Curve (c) is then the result of imposing cosmic-ray rejection, escaped radiation correction, and pulse-pileup rejection on spectrum (b).

Data were accumulated event by event on magnetic tape. At the same time, a gamma-ray spectrum histogram was accumulated in real time subject to conditions imposed by the time-of-flight condition, the pileup suppression circuit, a veto condition imposed by events in the plastic scintillators, and a high level discriminator setting which was set so as to eliminate the region of fixed-energy gamma rays ( $< \sim 20$  MeV) from the histogram. Typical spectra of the various reactions studied, showing the line-shape analysis of transitions to the various ground states ( $\gamma_0$ ) and low-lying excited states, are shown in Fig. 2. A software window was placed on the gamma-ray peak in the time-of-flight spectrum allowing the sorting algorithm of the data acquisition system to select only the gamma rays from the events recorded. It is important to note that the events shown in the various spectra are capture  $\gamma$  rays and not a "background." With the exclusion of neutrons from the spectra, only capture  $\gamma$  rays have sufficient energy to appear in the high-energy region of the spectrum. All charged particles resulting from reactions in the target which enter the NaI crystal are rejected from the spectra by the anticoincidence condition on the plastic scintillator at the front of the  $\gamma$ -ray detector, as are any subsequent events induced by charged-particle reactions in the plastic which then enter the crystal. A relatively complete stripping of a spectrum is shown for the  $^{27}\text{Al}(p,\gamma)$  reaction. The large rise in yield at  $E_x \sim 12$  MeV is due to the lower discriminator setting for this run, which permitted fixed-energy reaction  $\gamma$  rays at energies below 15 MeV to enter the spectrum.

Off-line sample histograms were reconstructed event by event from the event tapes for comparison with the on-line histogram. A two-parameter histogram was also generated, with the  $x$  axis corresponding to the energy deposited in the NaI crystal and the  $y$  axis to the energy deposited in the plastic annulus. A resum algorithm was used to build a histogram composed of valid  $\gamma$ -ray events rejected by the plastic. This algorithm adds the energy deposited in the plastic scintillator to that detected in the central crystal, thereby providing first-order corrected spectra which compensate for counting losses arising from the anticoincidence condition. The cross section calculations then include the resum correction

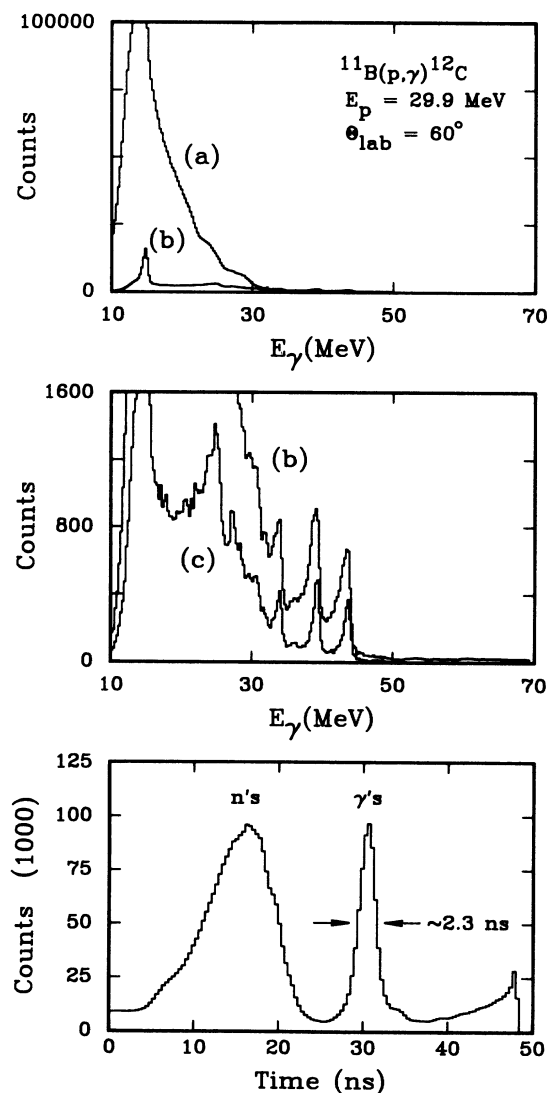


FIG. 1. Curve (a) is the raw NaI spectrum and includes both neutrons and  $\gamma$  rays. Curve (b), shown on two different scales, is the resultant NaI spectrum after neutrons were rejected by placing a software window on the  $\gamma$ -ray peak shown in the time-of-flight spectrum in the bottom panel. Curve (c) is the final  $\gamma$ -ray spectrum after imposing cosmic-ray and escaped-radiation corrections.

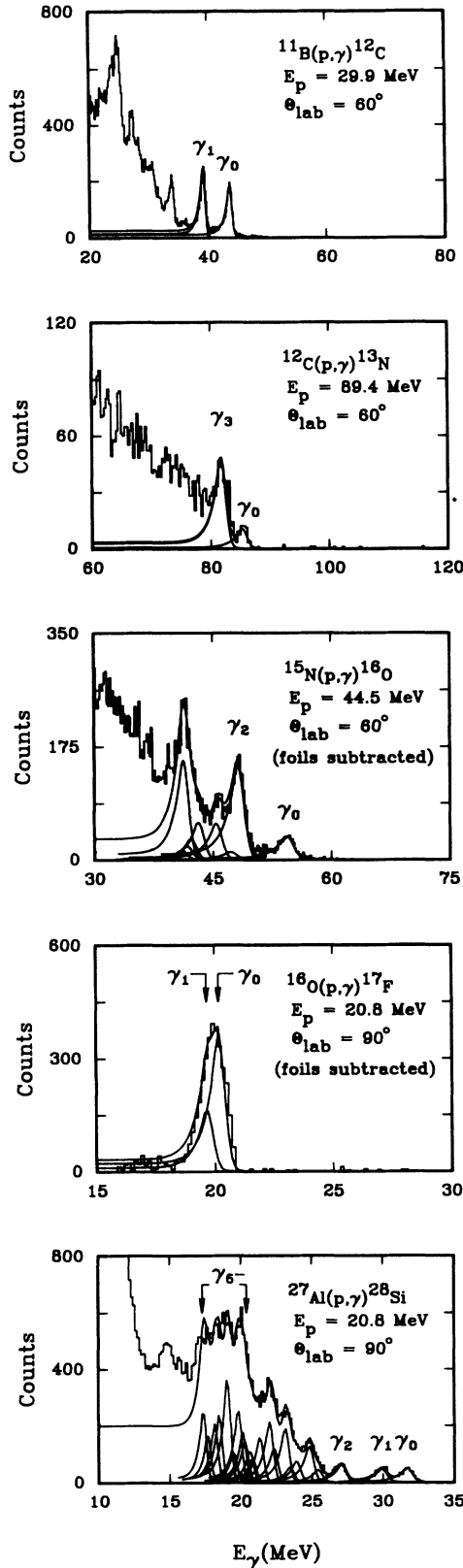


FIG. 2. Gamma-ray spectra of  $(p,\gamma)$  reactions on five nuclear species measured at various bombarding energies. The solid curves in the figures are line-shape fits to the spectra.

factor. Last, a histogram of LED pulses was also accumulated as a check on the operation of the gain stabilization system. The LED pulses were recorded on the event tapes along with the NaI and plastic scintillator events.

Differential cross sections were calculated after first stripping our gamma-ray histogram utilizing an empirically determined line shape.<sup>1</sup> The line shape consists of a Gaussian form on the high-energy side of the full-energy peak which joins smoothly onto a decaying exponential on the low-energy side of the peak. In turn, the decaying exponential joins smoothly to a constant value which extends to zero energy. A spectrum was stripped, using the empirical line shape, peak by peak from the highest energy region of the spectrum. The areas so determined were then corrected for pulse pileup, computer dead time, the resum factor, and a time-of-flight correction.

The differential cross sections were obtained from the expression

$$N(\gamma) = \left[ \frac{d\sigma}{d\Omega} \right] QNC d\Omega_\gamma,$$

where  $N(\gamma)$  is the number of gamma rays in the stripped spectrum obtained for an accumulated charge  $Q$ ,  $N$  is the number of scattering centers,  $d\Omega_\gamma$  is the solid angle of the  $\gamma$ -ray detector, and  $C$  is a correction factor accounting for pulse pileup, computer dead time, a time-of-flight correction for events lost due to rarely occurring cyclotron radio frequency (rf) phase shifts, and the resum factor. The efficiency of the  $\gamma$ -ray detector is assumed to be essentially 100%, and the uncertainty in this efficiency is included in the resum-factor uncertainty ( $\sim 15\%$ ).

The analyzing power measurements were carried out using the IUCF fast spin-flip mode of operation. In this mode the beam polarization was periodically reversed between spin up and spin down while synchronizing the data acquisition with the spin states. The time between spin reversals were fixed at 60 s. For the majority of our polarized beam runs, a polarimeter was placed in the low-energy beam line between the injector stage and the main stage of the cyclotron. The polarimeter contained a  $^4\text{He}$  gas cell which could be moved in and out of the proton beam under command of the cyclotron control system. (For a few of the runs, at the lowest energies, a polarimeter in the beam line directly in front of our target was utilized.) The beam polarization was measured periodically during an experiment and typically had a value of 0.70–0.75. Analyzing powers were then calculated with the detector on the *right-hand side* of the beam line, using the Basel convention, as

$$A_y = \frac{N\downarrow - N\uparrow}{N\downarrow|P\uparrow| + N\uparrow|P\downarrow|},$$

where  $N\downarrow$  and  $N\uparrow$  are the number of gamma-ray events and  $P\downarrow$  and  $P\uparrow$  the beam polarizations in the spin down and spin up modes, respectively.

The  $\pm 20\%$  uncertainty associated with the cross section measurements are primarily due to the uncertainties

associated with stripping the spectra,  $\lesssim \pm 15\%$ , and with the resum correction,  $\lesssim \pm 15\%$ ; the uncertainties associated with target thickness and uniformity, charge collection, and solid angle were small compared to these.

### III. RESULTS

#### A. The $^{11}\text{B}(p,\gamma)^{12}\text{C}$ reaction

The  $^{11}\text{B}(p,\gamma)$  reaction is the one we have studied the most extensively in the energy range of 20 to 100 MeV.

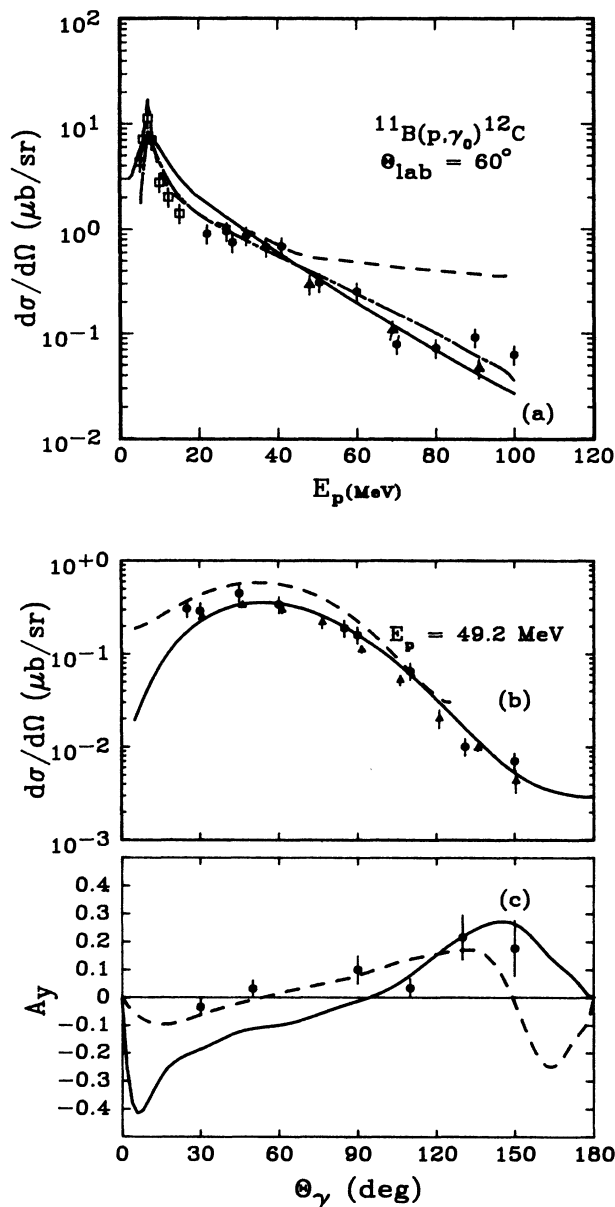


FIG. 3. The energy dependence of the  $60^\circ$  differential cross section for  $^{11}\text{B}(p,\gamma)^{12}\text{C}$  is shown in (a). The differential cross section and analyzing power angular distributions are shown in (b) and (c), respectively. The dashed and dot-dashed curves are from DSD calculations with energy-dependent and fixed OMP's, respectively. The solid curves are from the relativistic model calculations of Ref. 23. The square data points are from Ref. 8 and the triangular data points from Ref. 5.

The reasons for this are partly experimental: self-supporting targets of enriched  $^{11}\text{B}$  can be prepared at controlled thicknesses, the  $Q$  value of the  $(p,\gamma)$  reaction is large and positive—giving the highest  $\gamma$ -ray energy for the incident proton energy—the separation in energy of the  $\gamma$  rays populating the ground and 4.44 MeV first-excited state is large, and the reaction cross section is large. As noted in the Introduction, as we studied this reaction, further interesting effects appeared, thereby increasing our concentration in this particular  $(p,\gamma)$  reaction. In Fig. 2,  $\gamma$  rays populating the  $^{12}\text{C}$  ground ( $\gamma_0$ ) and first-excited state ( $\gamma_1$ ) are well resolved from one another at  $E_p = 29.9$  MeV. At all the bombarding energies studied, the  $\gamma$  rays populating the ground state were sufficiently resolved from those populating the 4.44 MeV excited state so that the ground state yield could be adequately stripped from the spectra.

The energy dependence of the  $\theta_\gamma = 60^\circ$   $(p,\gamma_0)$  cross section is shown in Fig. 3. Also shown in the figure are cross sections calculated using detailed balance from the  $^{12}\text{C}(\gamma,p_0)^{11}\text{B}$  reaction reported by Mathews *et al.*<sup>5</sup> at  $E_\gamma = 60, 80,$  and  $100$  MeV. In the vicinity of the giant dipole resonance (GDR) centered at  $E_p = 7.5$  MeV, data points are plotted from the work of Allas *et al.*<sup>8</sup>

The dashed curve in Fig. 3 was calculated using the direct-semidirect program HIKARI,<sup>9</sup> described in Sec. IV, using an energy-dependent set of optical model parameters (OMP's) and a spectroscopic factor of 5.69 obtained from the calculations of Cohen and Kurath.<sup>10</sup> The dot-dashed curve in the figure was also calculated using

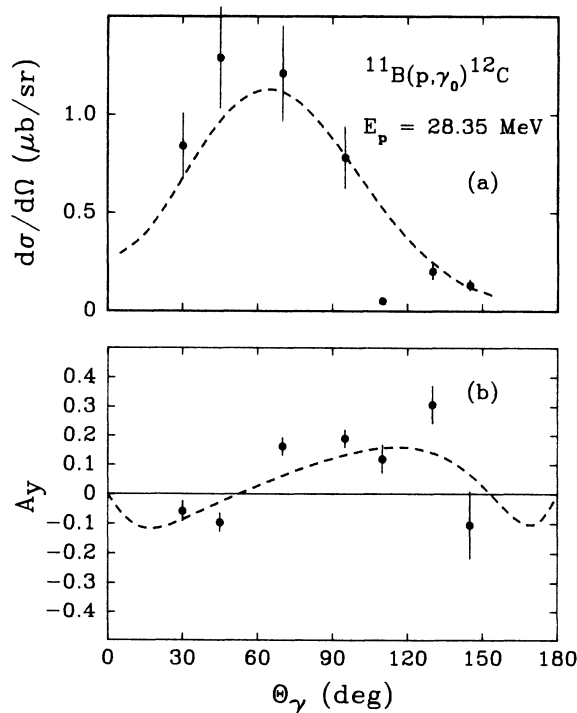


FIG. 4. The  $^{11}\text{B}(p,\gamma)^{12}\text{C}$  differential cross section (a) and analyzing power (b) angular distributions measured at  $E_p = 28.35$  MeV. The curves in the figures are DSD calculations.

HIKARI and the appropriate spectroscopic factor, but the OMP's were fixed at  $E_p = 20$  MeV. This point will be discussed later. The solid curve in the figure was calculated using the model of McDermott *et al.*<sup>11</sup> described in Sec. IV. Also included in Fig. 3 are the angular distributions and analyzing powers measured at  $E_p = 49.2$  MeV. We have included data points in the angular distributions, calculated using detailed balance, from Mathews *et al.*<sup>5</sup> for the  $E_\gamma = 60$  MeV  $^{12}\text{C}(\gamma, p_0)^{11}\text{B}$  reaction at approximately the same  $\gamma$ -ray energy region as for our data,  $E_\gamma = 62.1$  MeV at  $\theta_\gamma = 60^\circ$ . Two model calculations are shown in the figure; as before, the dashed curves were calculated using HIKARI, and the solid curves were calculated using the model of McDermott *et al.* An additional angular distribution and analyzing power measurement, taken at  $E_p = 28.35$  MeV, is shown in Fig. 4. The curves on that figure are calculated with HIKARI.

### B. The $^{12}\text{C}(p, \gamma_0)^{13}\text{N}$ reaction

Proton captures into the closed subshell plus one proton nucleus  $^{13}\text{N}$  were measured at seven energies between 28.35 and 90 MeV. A spectrum of the  $^{12}\text{C}(p, \gamma)$  reaction is shown in Fig. 2. Even at  $E_p = 90$  MeV, the  $\gamma$  rays from proton captures populating the ground state ( $\gamma_0$ ) of  $^{13}\text{N}$  are resolved from excited state capture  $\gamma$  rays. The energy dependence of the  $60^\circ$   $^{12}\text{C}(p, \gamma_0)^{13}\text{N}$  differential cross sections is shown in Fig. 5. The data points plotted in the vicinity of the GDR, centered at approximately 20 MeV, are from the work of Berghofer *et al.*<sup>12</sup> taken at a detector angle of  $90^\circ$ . The dashed curve in the figure was calculated using the DSD model with energy varying OMP's and a spectroscopic factor of 0.61 obtained from the calculations of Cohen and Kurath. The solid curve in the figure was calculated with the OMP's fixed. The results of angular distribution and analyzing power measurements taken at a bombarding energy of 28.35 MeV are also shown in Fig. 5.

### C. The $^{15}\text{N}(p, \gamma_0)^{16}\text{O}$ reaction

Both the  $^{15}\text{N}(p, \gamma)$  and  $^{16}\text{O}(p, \gamma)$  reactions were measured using the gas cell described earlier. Consequently, the raw spectra contained  $\gamma$  rays from the entrance and exit Havar foils. To determine these contributions in the total spectrum, we performed runs with the gas cell completely evacuated. The spectrum of  $\gamma$  rays from the foils showed no resolvable structure and was monotonically decreasing with increasing  $\gamma$ -ray energy. The empty gas cell runs were normalized to the gas-filled runs by charge integration and their contributions were subtracted point by point from the gas-filled cell spectra. A  $\gamma$ -ray spectrum from the  $^{15}\text{N}(p, \gamma)$  reaction taken at an angle of  $60^\circ$  is shown in Fig. 2. Gamma rays from the proton captures populating the ground state ( $\gamma_0$ ) of the doubly closed-shell nucleus  $^{16}\text{O}$  are well resolved from higher excited states at all bombarding energies studied.

The energy dependence of the  $60^\circ$  ground state differential cross sections for this reaction is shown in Fig. 6. Also shown in the figure are cross sections calcu-

lated using detailed balance from the  $^{16}\text{O}(\gamma, p_0)^{15}\text{N}$  reaction reported by Findlay and Owens<sup>6</sup> for  $E_\gamma = 60, 80,$  and  $100$  MeV. The data points in the vicinity of the GDR, centered at a bombarding energy of 12 MeV, were taken from the paper by Baglin and Thompson.<sup>13</sup> As before, the dashed curve in the figure is the DSD model calculation using energy-dependent OMP's; the spectroscopic factor here is 3.2, which is an average of spectroscopic factors reported from ( $^3\text{He}, d$ ) measurements on  $^{15}\text{N}$ . The dot-dashed curve is the DSD model calculation with fixed OMP's; the solid curve is due to the model of McDermott *et al.*

Included in Fig. 6 are the angular distributions and analyzing power measurements taken at  $E_p = 49.6$  MeV. Additional data points in the angular distributions, calculated using detailed balance, are taken from Findlay

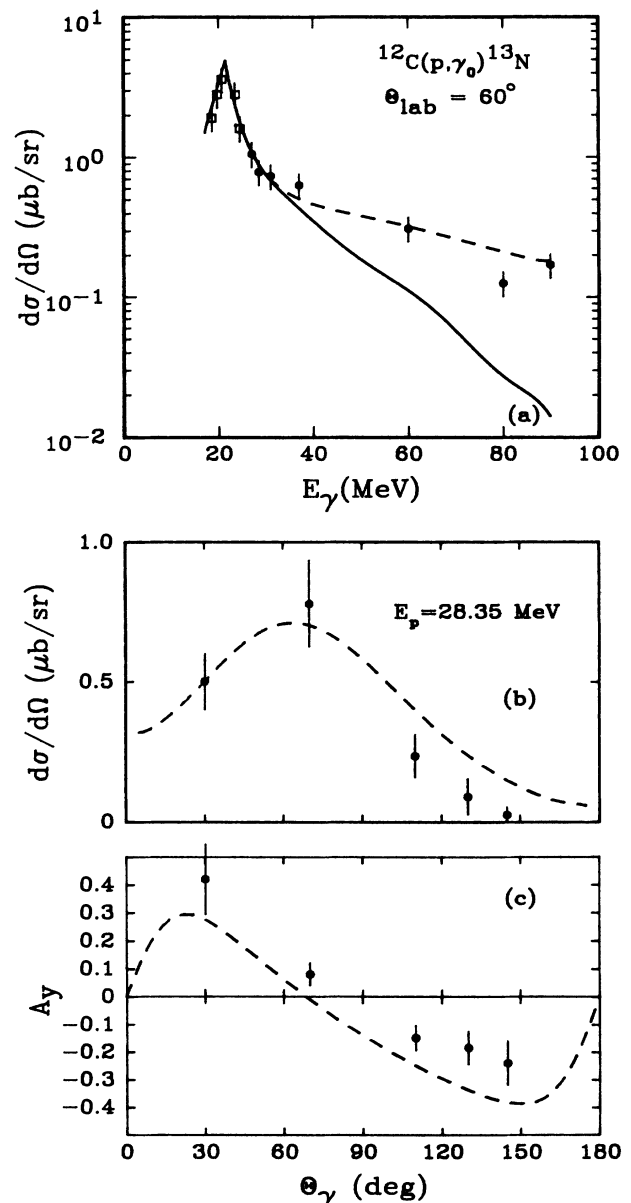


FIG. 5. Same as Fig. 3 for  $^{12}\text{C}(p, \gamma_0)^{13}\text{N}$ . The square data points are from Ref. 12.

and Owens<sup>6</sup> for the  $E_\gamma = 60$  MeV  $^{16}\text{O}(\gamma, p_0)^{15}\text{N}$  reaction at approximately the same  $\gamma$ -ray energy as for our data,  $E_\gamma = 59.2$  MeV at  $\theta_\gamma = 60^\circ$ . Two model calculations are shown in the figure: the dashed curve using the DSD program HIKARI and the solid curve using the model of McDermott *et al.*

#### D. The $^{16}\text{O}(p, \gamma_0)^{17}\text{F}$ reaction

A spectrum of  $\gamma$  rays from proton captures populating states in the closed shell plus one proton nucleus  $^{17}\text{F}$  is shown in Fig. 2 for a bombarding energy of 20.8 MeV. The energy dependence of the  $60^\circ$  differential cross sections was measured at only three energies and is shown

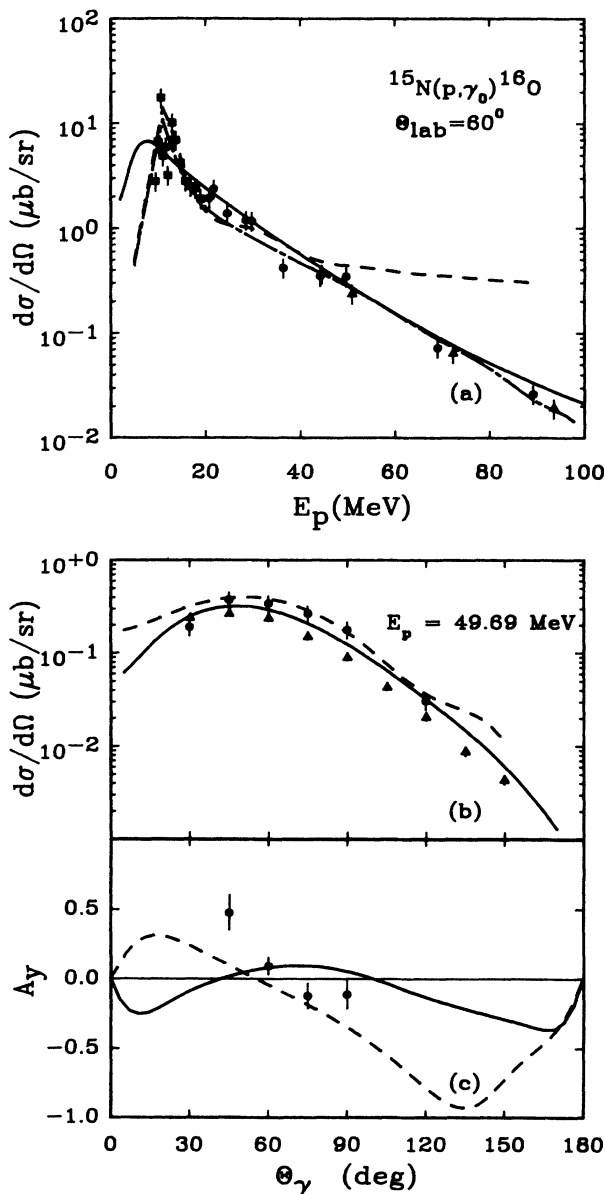


FIG. 6. Same as Fig. 3 for  $^{15}\text{N}(p, \gamma_0)^{16}\text{O}$ . The square data points are from Ref. 13 and the triangular data points from Ref. 6.

in Fig. 7. Additional data points in the vicinity of the GDR centered at  $E_p = 22$  MeV were obtained from the paper by Harakeh, Paul, and Gorodetzky<sup>14</sup> at a  $\gamma$ -ray detector angle of  $90^\circ$ . The dashed curve in the figure was again calculated using energy-dependent OMP's and, here, a spectroscopic factor of 0.94 obtained from the literature. The dot-dashed curve was calculated using fixed OMP's. The differential cross sections and analyzing powers were measured for only two angles at a bombarding energy of 20.8 MeV and are also shown in Fig. 7. It is difficult to draw a meaningful conclusion about the agreement between calculations and measurement for a two-point angular distribution, except to note that the calculations are not inconsistent with the measurements.

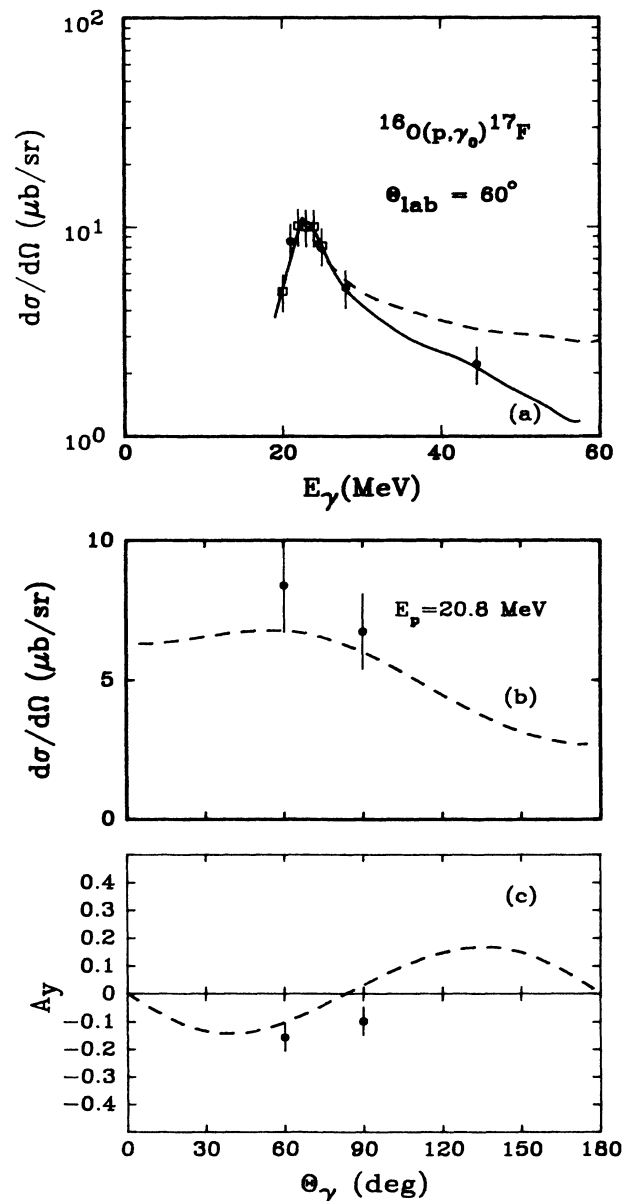


FIG. 7. Same as Fig. 3 for  $^{16}\text{O}(p, \gamma_0)^{17}\text{F}$ . The square data points are from Ref. 14.

### E. The $^{27}\text{Al}(p,\gamma_0)^{28}\text{Si}$ reaction

The  $^{27}\text{Al}(p,\gamma)$  reaction was measured at seven energies between  $E_p = 20.8$  and 80 MeV. A spectrum of  $\gamma$  rays for this reaction, taken at a bombarding energy of 20.8 MeV, is shown in Fig. 2. Gamma rays from the proton captures populating the ground ( $\gamma_0$ ), first-excited ( $\gamma_1$ ), and second-excited ( $\gamma_2$ ) states in  $^{28}\text{Si}$  are resolved from one another.

The energy dependence of the  $60^\circ$  differential cross sections is shown in Fig. 8. Additional data points in the vicinity of the GDR, centered at an energy of 8.5 MeV, were obtained from the paper by Singh *et al.*<sup>15</sup> at a detector angle of  $90^\circ$ . The dashed curve in the figure was again calculated using the DSD model with energy-dependent OMP's and, for this reaction, with an average

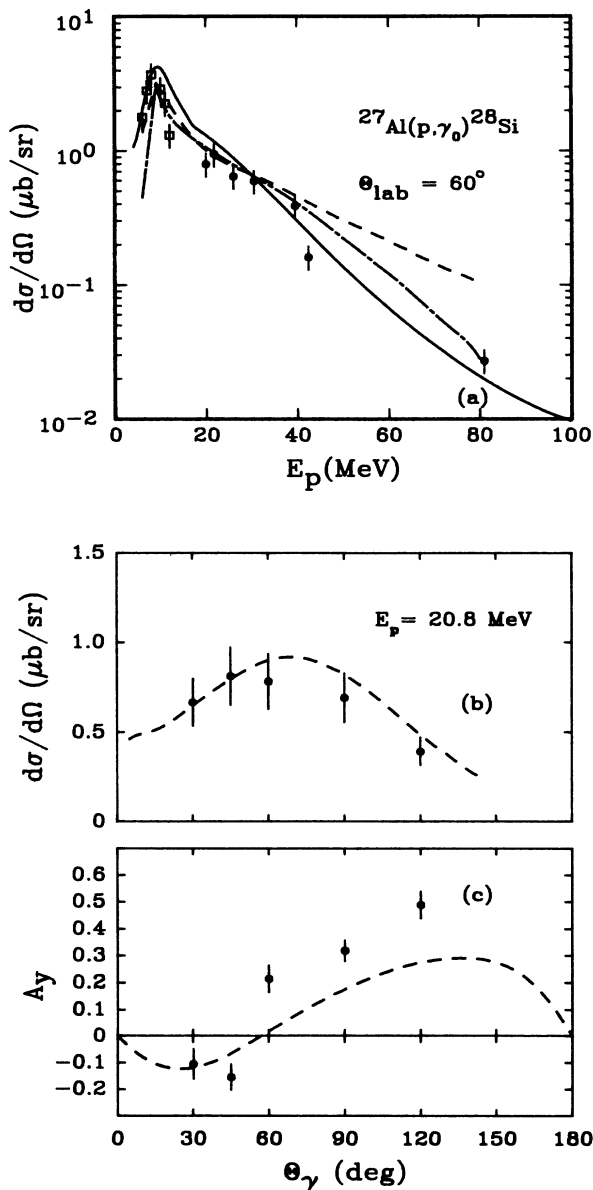


FIG. 8. Same as Fig. 3 for  $^{27}\text{Al}(p,\gamma_0)^{28}\text{Si}$ . The square data points are from Ref. 15.

spectroscopic factor of 4.15 obtained from ( $^3\text{He},d$ ) and ( $d,n$ ) measurements reported in the literature. The dot-dashed curve was calculated with the OMP's fixed; the solid curve in the figure was calculated using the model of McDermott *et al.*

The angular dependence of the differential cross sections and analyzing powers, measured at a proton bombarding energy of 20.8 MeV, is also shown in Fig. 8. The curves in the figures were calculated using HIKARI. No calculations using the relativistic model were attempted in this low energy region.

## IV. MODEL CALCULATIONS

### A. Direct-semidirect calculations

The DSD reaction model for describing radiative capture of fast nucleons, first proposed by Brown<sup>16</sup> and modified by Lushnikov and Zaretsky,<sup>17</sup> by Clement, Lane, and Rook,<sup>18</sup> and by Potaker *et al.*,<sup>19</sup> has had success in describing ( $p,\gamma$ ) and ( $n,\gamma$ ) capture cross sections, particularly in the region of the GDR. In these DSD models, the transition amplitude is the coherent sum of two terms. Using a projection operator formalism,<sup>20</sup> where  $P$  is the projection operator which projects from the space of the nuclear Hamiltonian that part which corresponds to a nucleon coupled to the target ground state, and  $Q$  is the complement of  $P$ , the transition amplitude can be expressed as

$$M = \langle P\psi_f | H^\lambda | P\psi_i \rangle + \langle P\psi_f | H^\lambda | Q\psi_i \rangle,$$

where the initial state  $\psi_i$  and the final state  $\psi_f$  are eigenstates of a nuclear Hamiltonian  $H$  with energies  $E_i$  and  $E_f$ , respectively, and  $H^\lambda$  is the electromagnetic interaction Hamiltonian which acts as a transition operator for the creation of a photon with energy  $E_\gamma = E_i - E_f$  and helicity  $\lambda$ . The first term is the direct-capture amplitude and the second term represents a two-step process where  $Q\psi_i$  is approximated by a single state which represents a nucleon coupled to a coherent one-particle one-hole excitation of the target ground state. The radial part of the semidirect amplitude is calculated according to

$$\langle u | h^L(r) | u' \rangle \frac{1}{(E_\gamma - E_R + i\Gamma/2)},$$

where  $u'$  and  $u$  are the initial and final radial wave functions, respectively, of the nucleon being captured from a continuum state into a bound single-particle orbital,  $h^L(r)$  is the form factor responsible for the inelastic excitation of the collective state (the GDR) by the incoming nucleon, and  $E_R$  and  $\Gamma$  refer to the position and width, respectively, of the resonance. In the present work only the isovector GDR was included in the calculations. The form factor was assumed to have a volume shape for electric dipole transitions

$$h^{E1}(r) \propto V_1 r f(r),$$

where  $V_1$  is the real part of the symmetry term in the optical potential and  $f(r)$  is the Woods-Saxon form factor. The geometry factors were taken from the optical-

TABLE I. Bound state parameters for the DSD calculations. Energies are in MeV and the nuclei listed are the product nuclei.

	$^{12}\text{C}$	$^{13}\text{N}$	$^{16}\text{O}$	$^{17}\text{F}$	$^{28}\text{Si}$
$S$	5.69	0.61	3.2	0.94	4.85
GDR (energy)	22.60	20.40	22.44	22.0	19.6
GDR (width)	3.2	3.5	3.0	3.5	4.3
EWSR	0.9	0.8	0.9	0.65	0.9
$V_1$ (at GDR)	61.36	57.08	59.63	54.85	60.22

model parameters of Watson, Singh, and Segel<sup>21</sup> for the  $1p$  shell nuclei,  $^{11}\text{B}$ ,  $^{12}\text{C}$ ,  $^{15}\text{N}$ , and  $^{16}\text{O}$ ; for the  $^{27}\text{Al}$  calculations the optical model parameters of Menet *et al.*<sup>22</sup> were used. The parameters used in the DSD calculations are contained in Table I. These calculations included direct  $E1$  and semidirect strength from the isovector GDR and direct  $E2$  only. The computer code HIKARI (Ref. 9) was used to perform the DSD model calculations. In this program the spectroscopic factor for the reaction appears as an overall normalization. Values of the spectroscopic factor for the transfer of a proton were obtained from the literature, as described earlier.

An isoscalar giant quadrupole resonant term was originally included in the  $^{13}\text{N}(p,\gamma)$  calculations. However, its contribution to the energy-dependent cross sections proved to be very small and such terms are not included in the DSD calculations presented here.

### B. A relativistic model calculation

The relativistic calculations were performed by McDermott<sup>23</sup> from a model by McDermott *et al.*<sup>11</sup> This model uses four-component Dirac wave functions and includes single particle and pion exchange mechanisms with direct and semidirect processes in each mechanism. These calculations are quite preliminary; since no complete set of relativistic optical-model parameters exist as yet in this energy region, a distorted-wave impulse approximation (DWIA) was used to calculate the continuum wave functions for the incident unbound protons. Although it is generally thought to be inappropriate to use the DWIA in this energy region, it was considered to be the best approach for these preliminary calculations. In addition, these calculations contain a single energy-independent parameter for the semidirect mechanism which was fitted to the differential cross section at  $E_\gamma = 60$  MeV.

## V. DISCUSSION

Our assumption, within the solid angle it subtends, that the efficiency of our NaI detector system is essentially 100% is based on the expectation that every photon (within a few percent) entering the NaI crystal deposits some energy in the crystal. For 100 MeV  $\gamma$  rays, only  $\sim 7.5$  radiation lengths ( $\sim 19.4$  cm of NaI) are required to contain the full-energy shower. If the full shower is captured in the NaI crystal, the event appears in the full-energy peak in the spectrum; if partial energy is deposited in the crystal and additional energy is de-

posited in the plastic annulus, we recover the event from our two-dimensional array; finally, if some of the shower escapes from the rear of the assembly where no plastic exists, the event appears in the tail of our line shape. The  $\pm 20\%$  uncertainty we then assign to our absolute cross sections, as noted earlier, is associated primarily with the uncertainties associated with our escaped radiation ("resum") correction and with the unknown tail of the line shape, which introduces uncertainties into the spectrum stripping process. We are encouraged that this procedure is reasonable by the comparison of our absolute cross sections with the cross sections, calculated by detailed balance, of the  $^{12}\text{C}(\gamma, p_0)$  and  $^{16}\text{O}(\gamma, p_0)$  results of Refs. 5 and 6 measured at  $E_\gamma = 60, 80,$  and  $100$  MeV. The small discrepancies which remain between the absolute cross sections of our  $(p, \gamma_0)$  and the  $(\gamma, p_0)$  results are, at least, partially understandable from the fact that the measurements were not made at exactly the same  $\gamma$ -ray energies, and are in a region where the  $60^\circ$  differential cross sections do have a strong energy dependence.

For the DSD calculations described above we provided as input to the program HIKARI an energy-dependent set of OMP's,<sup>21</sup> which were obtained from proton elastic scattering measurement on  $1p$  shell nuclei in the energy range of 10 to 50 MeV, in order to calculate the radial wave functions for the unbound continuum protons. In the vicinity of the GDR, we included data points from the literature in order to adjust the value of the energy-weighted sum-rule (EWSR) parameter in the program to fit the envelope of the GDR. Up to a proton bombarding energy of  $\sim 50$  MeV, the DSD calculations provided a reasonable description of the measurements in shape, if not always in magnitude. It must be noted that we did not adjust the OMP's to provide a better fit to the data. Above a bombarding energy of 50 MeV we extrapolated the energy dependence of the OMP's outside the energy region for which they were determined. As can be seen in the figures this resulted in the DSD calculations giving results as much as an order of magnitude greater than some of the measurements at  $E_p \sim 100$  MeV. At present, we are uncertain as to whether this is a breakdown in the applicability of the DSD model or an inappropriate extrapolation of the OMP's.

We found, rather fortuitously, that if we fixed the OMP's at their values near the energy of the GDR, the DSD calculations give a reasonable description of the energy dependence of the  $60^\circ$  differential cross section for four out of the five data sets over the complete energy region studied. This point has been addressed earlier

in a paper by Fink, Hebach, and Kummel,<sup>24</sup> who argued that if one used nonorthogonal continuum and bound-state wave functions to describe the interaction, an energy-dependent set of OMP's could always be found that would lead to fits to the experimental data then available, but would lead to no basic understanding of the physics underlying the interaction. While we can state no physical reasons as to why such agreement occurs, we have included the calculations as a point of interest.

In the energy region still dominated by the GDR at  $E_p = 20.8$  and  $28.35$  MeV, the DSD model with an energy-dependent global set of OMP's provides a reasonable description of the shape of the analyzing-power angular distributions. Even at the highest energy,  $E_p \sim 50$  MeV, the DSD model again provides a reasonable description of the analyzing-power angular distributions in shape, if not in magnitude. It is possible that by varying the OMP's somewhat, a better fit to the analyzing powers could have been obtained. However, we did not feel that this procedure would have enhanced our understanding of the reaction. The relativistic model analyzing power calculations of McDermott were performed

only at the highest energy,  $E_p \sim 50$  MeV.

In general, both models available to us gave reasonable descriptions of the energy dependence and angular distributions of the differential cross sections. However, the present relativistic model calculations had neither the shape nor the magnitude of the analyzing power measurements. The fact that the relativistic model, even with questionable wave functions for this energy region, gives quite good agreement with cross section data, but not with analyzing powers, indicates that analyzing power data provide a more critical test of the details of these reaction models than do cross section data alone. We look forward to the eventual availability of more rigorous relativistic calculations.

#### ACKNOWLEDGMENTS

The authors are indebted to Dr. Joseph P. McDermott for providing us his preliminary calculations prior to publication. We thank Professor Henry R. Weller for the use of the DSD program HIKARI. This work was supported in part by the National Science Foundation under Grant PHY-8504733.

- 
- <sup>1</sup>M. A. Kovash, S. L. Blatt, R. N. Boyd, T. R. Donoghue, H. J. Hausman, A. D. Bacher, and C. C. Foster, *Phys. Rev. Lett.* **42**, 700 (1979); M. A. Kovash, Ph.D. dissertation, The Ohio State University, 1978.
- <sup>2</sup>H. R. Weller, H. Hasan, S. Manglos, G. Miter, N. R. Robertson, S. L. Blatt, H. J. Hausman, R. G. Seyler, R. N. Boyd, T. R. Donoghue, M. A. Kovash, A. D. Bacher, and C. C. Foster, *Phys. Rev. C* **25**, 2921 (1982).
- <sup>3</sup>A. Anghinolfi, P. Corvisiero, G. Ricco, M. Taiuti, and M. Zucchiatti, *Nucl. Phys.* **A399**, 66 (1983).
- <sup>4</sup>D. Dowel, G. Feldman, K. Snover, A. Sandorfi, and M. Collins, *Phys. Rev. Lett.* **50**, 1191 (1983).
- <sup>5</sup>J. L. Matthews, D. J. S. Findlay, S. N. Gardiner, and R. O. Owens, *Nucl. Phys.* **A267**, 51 (1976).
- <sup>6</sup>D. J. S. Findlay and R. O. Owens, *Nucl. Phys.* **A279**, 385 (1977).
- <sup>7</sup>M. A. Kovash and S. L. Blatt, *Nucl. Instrum. Methods* **163**, 113 (1979).
- <sup>8</sup>R. G. Allas, S. S. Hanna, Luise Meyer-Schutzmeister, and R. E. Segel, *Nucl. Phys.* **58**, 122 (1964).
- <sup>9</sup>Hideo Kitazawa, Duke University report, 1980 (unpublished).
- <sup>10</sup>S. Cohen and D. Kurath, *Nucl. Phys.* **A101**, 1 (1967).
- <sup>11</sup>J. P. McDermott, J. R. Shepard, E. Rost, and C.-Y. Cheung (unpublished).
- <sup>12</sup>D. Berghofer, M. D. Hasinoff, R. Helmer, S. T. Lim, F. Measday, and K. Ebisawa, *Nucl. Phys.* **A263**, 109 (1976).
- <sup>13</sup>J. E. E. Baglin and M. N. Thompson, *Nucl. Phys.* **A138**, 73 (1969).
- <sup>14</sup>M. N. Harakeh, P. Paul, and Ph. Gorodetzky, *Phys. Rev. C* **11**, 1008 (1975).
- <sup>15</sup>P. P. Singh, R. E. Segel, L. Meyer-Schutzmeister, S. S. Hanna, and R. G. Allas, *Nucl. Phys.* **65**, 577 (1965).
- <sup>16</sup>G. E. Brown, *Nucl. Phys.* **57**, 339 (1964).
- <sup>17</sup>A. A. Lushnikov and D. E. Zaretsky, *Nucl. Phys.* **66**, 35 (1965).
- <sup>18</sup>C. F. Clement, A. M. Lane, and J. R. Rook, *Nucl. Phys.* **66**, 293 (1965).
- <sup>19</sup>M. Potokar, *Phys. Lett.* **46B**, 346 (1973); M. Potokar, A. Likar, M. Budnar, and F. Dvelbar, *Nucl. Phys.* **A277**, 29 (1977); M. Potokar, *Phys. Lett.* **92B**, 1 (1980).
- <sup>20</sup>S. L. Blatt, H. J. Hausman, L. G. Arnold, R. G. Seyler, R. N. Boyd, T. R. Donoghue, P. Koncz, M. A. Kovash, A. D. Bacher, and C. C. Foster, *Phys. Rev. C* **30**, 423 (1984).
- <sup>21</sup>B. A. Watson, P. P. Singh, and R. E. Segel, *Phys. Rev.* **182**, 977 (1969).
- <sup>22</sup>J. J. H. Menet, E. E. Gross, J. J. Malanify, and A. Zucker, *Phys. Rev. C* **4**, 1114 (1971).
- <sup>23</sup>J. P. McDermott, private communication.
- <sup>24</sup>M. Fink, H. Hebach, and H. Kummel, *Nucl. Phys.* **A186**, 353 (1972).